JSR
Publications

Available Online

J. Sci. Res. **17** (2), 441-456 (2025)

JOURNAL OF
SCIENTIFIC RESEARCH

www.banglajol.info/index.php/JSR

Thermo Diffusion Effects on MHD Unsteady Stagnation Point Nano Fluid Flow over an Exponentially Porous Stretching Sheet

R. Akter[1,2], M. D. Hossain[1], M. A. Islam[1,3,*], M. G. Hafez[1]

[1]Department of Mathematics, Chittagong University of Engineering and Technology, Chattogram 4349, Bangladesh

[2]Department of Natural Science, Port City International University, Chattogram 4217, Bangladesh

[3]Department of CSE, International Islamic University Chittagong, Chattogram 4318, Bangladesh

Received 28 August 2024, accepted in final revised form 16 February 2025

Abstract

An investigation employing numerical methods has been conducted to present the Soret effects on magnetohydrodynamic (MHD) Unsteady Stagnation Point nano fluid Flow over an exponentially porous stretching sheet in existence of joule heating, thermal radiation, viscous dissipation, time dependent heat source or sink, chemical reaction and suction or blowing. With the use of MATLAB's bvp4c solver, the leading time dependent PDEs may be reduced to a family of non-linear ODEs and numerically solved. The influence of relevant flow parameters on temperature, concentration and velocity distribution are demonstrated graphically. For different controlling parameters, Sherwood and Nusselt number along with the skin-friction coefficient are also tabulated. There is a fairly close agreement between the current outcome and the previously announced result.

Keywords: Nano fluid; Stagnation point; Time dependent heat source or sink; Thermophoresis; Soret.

© 2025 JSR Publications. ISSN: 2070-0237 (Print); 2070-0245 (Online). All rights reserved.

doi: https://dx.doi.org/10.3329/jsr.v17i2.75751 J. Sci. Res. **17** (2), 441-456 (2025)

1. Introduction

The study of nanofluid has acquired significant focus of scientist and researchers due to its several technological and industrial applications. Nanofluids are nanometer size solid particles and fibers sized 1-100 nm suspended in a base fluid. The commonly used solid particles are metallic solid such as copper, aluminium, silver and gold, non-metallic solid such as silicon, alumina etc. and metallic liquid such as sodium. On the other hand, oil, ethylene glycol mixture water and toluene are used as base fluids [1-3]. Choi and Eastman [4] first introduced the notion of the nanofluid to intensify the thermal conductivity of base fluid. Cui *et al.* [5] conducted a numerical investigation into the problem of boundary layer flow (BLF) of a nano fluid caused by an exponentially stretching sheet (ESS).

---

[*] *Corresponding author*: aminulislampciu88@gmail.com

Prasannakumara *et al.* [6] explored the behavior of nanofluids flowing through a porous ESS, considering factors such as a heat source/sink, thermophoretic particle deposition, and bioconvection. Amjad *et al.* [7] studied the flow of a tangent hyperbolic magnetohydrodynamic (MHD) nanofluid in a two-dimensional scenario across an ESS. Shamshuddin *et al.* [8] investigated the bioconvective behavior of reactive Casson hybrid nanofluid flow past an ESS, incorporating Ohmic heating and mixed convection effects. Ramesh *et al.* [9] examined the motion of a titanium oxide-iron oxide/ethylene glycol hybrid nanofluid over an ESS.

Fluid behavior at stagnation zones is governed by stagnation-point flow. Many other sectors and scientific fields can benefit from this exciting area of research. This flow pattern emerges when the fluid encounters a solid surface, and its velocity reaches zero at the point of stagnation. There have been several documented uses of the stagnation-point flow, such as in air purification and dentistry [10]. Rashid *et al.* [11] found the exact solution of Stagnation-Point Nano fluid Flow based copper-water over an ESS. Waini *et al.* [12] explored how radiation and MHD effects influence the flow towards a stagnation point on an exponentially shrinking sheet in a hybrid nano fluid. Meanwhile, Mahmood *et al.* [13] investigated the effects of nanoparticle aggregation on MHD mixed convective stagnation point flow.

Viscous dissipation is the term used for the conversion of water's mechanical energy into thermal and acoustic energy when it flows downward. To mitigate erosion, various streambed devices can be built to decrease the kinetic energy of flowing fluids [14]. Because radiative heat transfer has so many industrial and engineering applications including gas turbines, nuclear reactors, spacecraft, hypersonic flights, nuclear power plants, and the modeling of relevant equipment it is important to research radiative heat transfer. Thus, in the processes of heating and cooling, the combined impact of viscous dissipation and thermal radiation is important [15]. Because of its significance in engineering and industry, the study of Joule heating, commonly referred to as "Ohmic heating," has drawn attention from researchers. It arises from interactions between atomic ions within the conductor and moving charged particles responsible for current flow [16]. Furthermore, the phrase "non-uniform heat generation or absorption" refers to the time-dependent internal heat generation or absorption, which has significant uses in the design of several biomedical equipment, electronic chips, nuclear reactors and semi-conductor wafers [17,18]. Therefore, it is important to investigate the combine effects of viscous dissipation, joule heating, thermal radiation and time dependent heat source or sink. Nandeppanavar *et al.* [19] analyzed the effect of non-uniform heat source/sink on MHD flow of viscoelastic fluid over an impermeable stretching sheet in presence of magnetic field due to frictional heating. Ramandevi *et al.* [20] utilized the Cattaneo-Christov model to analyze heat transfer in Casson and Viscoelastic fluids flowing across a stretching sheet, while accounting for time-dependent heat source/sink effects. In a separate study, Hady *et al.* [21] investigated the flow and heat transfer behaviors of a viscous nanofluid over a surface that undergoes nonlinear stretching, while also accounting for the impact of thermal radiation. Investigating the MHD flow of Williamson fluid, Akter and Islam [22] explored the impact of suction or blowing, along with non-uniform heat source/sink conditions.

Due to their significance in many organic manufacturing developments, chemical reactions in coupled heat and mass transfer issues have received a lot of research in latest decades. Examples of these kinds of operations include the creation and dispersal of fog, freezing-related crop damage, food processing, cooling towers, and the supply of moisture and temperature over cultivated arenas and fruit tree orchards [23]. Thermophoresis is an effective technique for gathering particles in which microscopic particles move in the direction of a diminishing heat gradient. When minute particles are transferred from the sheet to the fluid, thermophoresis occurs. Numerous industrial uses, such as filters, combustion engines, and turbine blades, depend on these phenomena. [23,24]. In addition, the Soret effect has been used in mixes involving gases with very little molecular weight $\left(H_{2,}He\right)$ and for isotope separation [25]. Daniel *et al.* [26] focused on the numerical solution of unsteady MHD nanofluid over a linearly porous extended sheet and his study involved the effects of several governing parameters, such assuction, thermal radiation, chemical reaction, thermophoresis, viscous dissipation and Joule heating. Raghunath [27] conducted a study focusing on the numerical solution of unsteady MHD flow. The study specifically examined water-based nanofluids containing Cu and TiO_2 flowing over an extended sheet. Thermal radiation, Soret effect, and chemical reaction were all taken into consideration in the investigation. Gohain *et al.* [28] analyzed the problem of MHD flow of water-based nanofluid past an infinite vertical porous plate and found that Soret number increases hydro magnetic and solutal boundary layer.

In this paper, we extend the earlier model proposed by Kumar *et al.* [29]. The extension incorporates stagnation point flow and porous medium effects in the momentum equation. Additionally, joule heating and viscous dissipation are accounted for in the energy equation. Furthermore, the diffusion equation now considers the Soret effect and chemical reaction. This study contributes to filling a gap in the existing literature. It employs similarity transformations to reduce the governing equations into nonlinear ODEs. These ODEs are subsequently solved numerically using the MATLAB solver bvp4c.

2. Mathematical Formulation of the Problem

In this analysis, the characteristics of an unsteady, two-dimensional flow are examined. The flow is laminar, electrically conducting, and involves chemical reactions within a nanofluid. Additionally, the flow is incompressible and directed towards a sheet experiencing exponential stretching with x and y axes aligned lengthwise and upright to the sheet, respectively. We suppose that $U=\frac{U_0 e^{x/L}}{1-\alpha t}$ denotes the stretching sheet velocity, $u_e=\frac{U_\infty e^{x/L}}{1-\alpha t}$ denotes the ambient fluid velocity, $T_w=T_\infty+\frac{T_0 e^{x/L}}{1-\alpha t}$ denotes the temperature flow near the surface, $C_w=C_\infty+\frac{C_0 e^{x/L}}{1-\alpha t}$ denotes the concentration near the surface, $v_w=\frac{v_0 e^{x/L}}{\sqrt{1-\alpha t}}$ denotes the velocity of mass transfer and $B=\frac{B_0 e^{x/2L}}{\sqrt{1-\alpha t}}$ denotes the uniform magnetic field perpendicular to the sheet, where $U_0>0,\alpha,L,U_\infty,T_0,T_\infty,C_0,C_\infty,v_0,B_0$ are stretching rate along the x axis, flow unsteadiness parameter, characteristic length, free stream velocity, reference temperature, ambient temperature, reference concentration, ambient concentration, constant mass flux velocity and initial magnetic field strength.

The continuity, momentum, energy and concentration equations governing the flow field are expressed as:

$$\frac{\partial u}{\partial x} + \frac{\partial v}{\partial y} = 0 \tag{1}$$

$$\frac{\partial u}{\partial t} + u\frac{\partial u}{\partial x} + v\frac{\partial u}{\partial y} = \nu\frac{\partial^2 u}{\partial y^2} + u_e\frac{du_e}{dx} - \frac{\sigma B^2}{\rho}(u - u_e) - \frac{\nu}{K_1}u \tag{2}$$

$$\frac{\partial T}{\partial t} + u\frac{\partial T}{\partial x} + v\frac{\partial T}{\partial y} = \alpha_m\frac{\partial^2 T}{\partial y^2} - \frac{1}{\rho C_p}\frac{\partial q_r}{\partial y} + \frac{\sigma B^2}{\rho C_p}u^2 + \frac{\mu}{\rho C_p}\left(\frac{\partial u}{\partial y}\right)^2 + \frac{1}{\rho C_p}q''' + \tau\left[D_B\frac{\partial C}{\partial y}\frac{\partial T}{\partial y} + \frac{D_T}{T_\infty}\left(\frac{\partial T}{\partial y}\right)^2\right] \tag{3}$$

$$\frac{\partial C}{\partial t} + u\frac{\partial C}{\partial x} + v\frac{\partial C}{\partial y} = D_B\frac{\partial^2 C}{\partial y^2} + \frac{D_T}{T_\infty}\frac{\partial^2 T}{\partial y^2} - K_r(C - C_\infty) + \frac{D_m K_T}{T_m}\frac{\partial^2 T}{\partial y^2} \tag{4}$$

Here ν stands for the kinematic viscosity, σ denotes the electric conductivity,κsignifies the thermal conductivity, T is the temperature of the fluid, q_r denotes the radiative heat flux, q''' signifies the non-uniform heat source or sink and (u, v) denote the velocity components along the x axis and y axis respectively. Additionally,$t$denotes the time, ρ denotes the density, C_p symbolizes the specific heat at constant pressure, τ denotes the ratio of nanoparticle material's heat capacity to the fluid's heat capacity and D_B, D_T denote the Brownian and the thermophoretic diffusion coefficients respectively.

The associated boundary conditions are:

$$u = U(x,t)\ ,\quad V = -V(x,t), T = T_w(x,t)\ , C = C_w(x,t)\ , at y = 0 \tag{5}$$

$$u \to 0, T \to T_\infty, C \to C_\infty as y \to \infty \tag{6}$$

The non uniform heat source or sink is defined by

$$q''' = \frac{\kappa U}{L\nu}[A_1(T_W - T_\infty)f' + B_1(T - T_\infty)]$$

Where A_1 and B_1 are space dependent and time dependent heat source or sink. $A_1, B_1 < 0$ and $A_1, B_1 > 0$ imply internal heat sink and source respectively.

The radiation heat flow q_r is expressed as follows after applying the Rosseland approximation [32]:

$$q_r = -\frac{4\,\sigma^*}{3K^*}\frac{\partial T^4}{\partial y} \tag{8}$$

The symbol K^* stands for the absorption coefficient, while σ^* denotes the Stefan-Boltzman constant. If we disregard the higher order parts in $(T - T_\infty)$ beyond the first degree and suppose that the flow's temperature difference in the flow is small enough for T^4 to be expanded in a Taylor's series about T_∞ known as free stream temperature, we obtain

$$T^4 \cong 4T_\infty^3 T - 3T_\infty^4.$$

Then the equation (3) becomes:

$$\frac{\partial T}{\partial t}+u\frac{\partial T}{\partial x}+v\frac{\partial T}{\partial y}=\frac{\kappa}{\rho C_p}\frac{\partial^2 T}{\partial y^2}+\frac{16\,\sigma^* T_\infty^3}{3\rho C_p K^*}\frac{\partial^2 T}{\partial y^2}+\frac{\sigma B^2}{\rho C_p}u^2+\frac{\mu}{\rho C_p}\left(\frac{\partial u}{\partial y}\right)^2+\frac{1}{\rho C_p}q''' \\ +\tau\left[D_B\frac{\partial C}{\partial y}\frac{\partial T}{\partial y}+\frac{D_T}{T_\infty}\left(\frac{\partial T}{\partial y}\right)^2\right] \tag{9}$$

The following dimensionless variables are introduced in order to solve the momentum, energy, and diffusion equations (2), (3), and (4).

$$\eta=\sqrt{\frac{U_0}{2\,\nu L(1-\alpha t)}}e^{x/2L}y\,,\qquad \psi=\sqrt{\frac{2\nu L U_0}{(1-\alpha t)}}e^{x/2L}f(\eta)$$

$$T=T_\infty+\frac{T_0}{(1-\alpha t)^2}e^{x/2L}\theta(\eta),\qquad C=C_\infty+\frac{C_0}{(1-\alpha t)^2}e^{x/2L}\phi(\eta) \tag{10}$$

Here, η denotes similarity variable and ψ denotes stream function; that is, $u=\frac{\partial\psi}{\partial y}$ and $v=-\frac{\partial\psi}{\partial x}$. The following system of ODEs results from inserting (10) into the equations (2) to (4):

$$f'''+ff''-2f'^2-A\left(\eta f''+2f'\right)+E^2-M\left(f'-E\right)-Kf'=0 \tag{11}$$

$$\left(1+\frac{4}{3}R\right)\theta''+\Pr\left(f\theta'-f'\theta\right)-\Pr A\left(4\theta+\eta\theta'\right)+\Pr Ec\left(f''\right)^2+\Pr Hf'^2+\Pr Q\theta \\ +\Pr\left(Nb\theta'\phi'+Nt\theta'^2\right)=0 \tag{12}$$

$$\phi''+\frac{Nt}{Nb}\theta''+\mathrm{Le}\left(f\phi'-f'\phi\right)-LeA\left(4\phi+\eta\phi'\right)-Le\gamma\phi+LeS_r\theta''=0 \tag{13}$$

Under the following Boundary conditions:

$$f(0)=S,f'(0)=1,\theta(0)=1,\phi(0)=1\quad \text{at}\eta=0$$
$$f'(\infty)\to 0,\theta(\infty)\to 0,\phi(\infty)\to 0\quad \text{as } \eta\to\infty$$

where, $A=\frac{\alpha L}{U_0 e^{x/L}}$ is the unsteadiness parameter, magnetic parameter is denoted by $M=\frac{2L\sigma B_0^2}{\rho U_o}$, $K=\frac{2L\,\nu}{K_0 U_0}$ is the porosity parameter, $E=\frac{U_\infty}{U_0}$ is the velocity ratio parameter, $\Pr=\frac{\rho C_p \nu}{\kappa}$ represents the Prandtl number, $\mathrm{R}=\frac{4\sigma^* T_\infty^3}{\kappa K^*}$ stands for the radiation parameter, $Ec=\frac{U^2}{C_p(T_f-T_\infty)}$ represents the Eckert number, $H=M.Ec$ represents the joule heating parameter, Brownian motion parameter is symbolized by $Nb=\frac{\tau D_B(C_w-C_\infty)}{\nu}$, $Nt=\frac{\tau D_T(T_w-T_\infty)}{T_\infty \nu}$ is the Thermophoresis parameter, $Le=\frac{\nu}{D_B}$ signifies the Lewis number, $\gamma=\frac{K_2 L}{U_0}$ and $S_r=\frac{D_m K_T T_0}{T_m C_0 \nu}$ stand for Chemical reaction parameter and Soret number, blowing or suction parameter is denoted by $\mathrm{S}=\frac{V_0}{\sqrt{\frac{U_0\,\nu}{2L}}}$ and the prime notation indicates the differentiation w.r.t. η.

In this area, what truly count are the Sherwood number, Nusselt number, and skin-friction coefficient. These parameters hold significant sway over the outcomes and analyses within this field. They are provided by

$$C_f = \frac{2\,\tau_w}{\rho\, U^2}, N_{u_x} = \frac{x\, q_w}{k(T_w - T_\infty)} \text{ and } S_{h_x} = \frac{\mathrm{x}\,\mathrm{J_w}}{\mathrm{D}\,(C_w - C_\infty)} \tag{15}$$

Where τ_w, q_w and $\mathrm{J_w}$ are the surface shear stress, surface heat flux and the mass flux respectively. They are given by

$$\tau_w = \mu \left(\frac{\partial u}{\partial y}\right)_{y=0}, q_w = -k \left(\frac{\partial T}{\partial y}\right)_{y=0} \text{ and } J_w = -D \left(\frac{\partial C}{\partial y}\right)_{y=0} \tag{16}$$

Substituting (13) into (12), we get

$$C_f = \sqrt{\frac{2x}{L}}(Re_x)^{-\frac{1}{2}} f''(0), N_{u_x} = -\sqrt{\frac{x}{2L}}\sqrt{Re_x}\,\theta'(0) \text{ and } S_{h_x} = -\sqrt{\frac{x}{2L}}\sqrt{Re_x}\,\phi'(0) \tag{17}$$

where $Re_x = \frac{x\,U}{\nu}$ is the local Reynolds number.

3. Methodology

The non-linear ODEs (7) and (8), alongside conditions (9), are worked out numerically using MATLAB's bvp4c solver. This solver employs the three-stage Lobatto IIIa collocation method, which guarantees a solution that is C1-continuous and maintains fourth-order accuracy across the entire integration range. Prior to applying this method, the original equations are transformed into a first-order system of ODEs.

$y_1 = f, y_2 = f', y_3 = f'', y_4 = \theta, y_5 = \theta', y_6 = \phi, y_7 = \phi'$

In MATLAB, a new set of variables is added as follows in order to find the numerical solution

$$y_2' = y_1$$

$$y_3' = y_2$$

$$y_3' = -y_1 y_3 + 2y_2^2 + A\;\;(2y_2 + \eta\, y_3) + E^2 - M(E - y_2) - Ky_2$$

$$y_4' = y_5$$

$$y_5' = \frac{1}{1 + \frac{4}{3}R}\begin{bmatrix} -\Pr(y_1 y_5 - y_2 y_4) + A\Pr(4y_4 + \eta\, y_5) - Ec\Pr y_3^2 - H\Pr y_2^2 \\ -2(A_1 y_2 + B_1 y_4) - \Pr(Nby_5 y_7 + Nty_5^2) \end{bmatrix}$$

$$y_6' = y_7$$

$$y_7' = -Le(y_1 y_7 - y_2 y_6) + Le\,A(4y_6 + \eta\, y_7) - Le\,\gamma\, y_6 + Le\,S_r y_5' - \frac{Nt}{Nb} y_5'$$

with associated boundary conditions

$y0(2) - 1 = 0, y0(1) - S = 0, y0(4) - 1 = 0, y0(6) - 1 = 0$

$yinf(2) = 0, yinf(4) = 0, yinf(6) = 0$

4. Results and Discussion

To visually depict the numerical data corresponding to equations (9) through (11) and the boundary condition (12), graphs and tables have been employed. These visual aids are constructed utilizing MATLAB's bvp4c solver for accurate solutions. For numerical estimation we consider the non-dimensional parameters as $A = A_1 = B_1 = Ec = 0.1, E = R = 0.2, H = Nb = S = \gamma = S_r = 0.3,$

$\eta = M = K = Nt = Le = 0.5, Pr = 7.$

The values remained unchanged throughout the study, with the exception of those presented in the figures and tables. No alterations were made to the values, except for those explicitly displayed in the figures and table. Table 1 shows a comparison between the results of Islam *et al.* [30] and Kumar *et al.* [29] and the values of Nusselt number for different values of Pr. For higher Prandtl number values, there is a close to good agreement. Table 2 compares the skin friction coefficient values for various M values with the findings of Kumar *et al.* [29] and Islam *et al.* [31], revealing a close and satisfactory agreement.

Table 1 Comparison of Nusselt Number for different values of Pr with $A = A_1 = B_1 = Ec = E = R = H = S = \gamma = S_r = \eta = M = K = Nt = Le = 0$ and $Nb = 0.001$.

Pr	Kumar *et al.* [29]	Islam *et al.* [30]	Present result
1	0.954853		1.3319
2	1.471445		1.6426
3	1.869062	1.9355	1.9338
5	2.500121	2.4684	2.4655
10	3.660344	3.5739	3.5680

Table 2: Evaluation of the skin friction coefficient for various values of M.

M	Kumar *et al.* [29]	Islam *et al.* [31]	Present result
0	-1.8049		-1.8049
0.5	-1.8851		-1.8851
1	-1.9627		-1.9627
2	-2.1109		-2.1109
5		-2.6592	-2.8692
10		-3.4617	-3.6501
50		-7.2126	-7.3623

The velocity$(f'(\eta))$, temperature$(\theta(\eta))$ and concentration$(\phi(\eta))$profiles are affected by the velocity ratio parameter (E), as shown in Figures 1-3. It's observed that with increasing E, the fluid velocity and concentration increase. However, the fluid temperature decreases despite these changes. Figs. 4-6 depict how the magnetic parameter (M) influences temperature, concentration, and velocity profiles. Fig. 4 unmistakably showcases the augmentation in fluid velocity as the parameter M ascends, aligning seamlessly with the expected impact of the Lorentz force created by the transverse magnetic field applied. This force acts resistively, slowing down fluid motion. Moreover, Fig. 5 illustrates the increase in fluid temperature as M grows, while Fig. 6 shows a corresponding decrease in the concentration profile with increasing M. Figs. 7- 9 elucidate how the $f'(\eta)$, $\theta(\eta)$e, and $\phi(\eta)$ profiles are affected by variations in the porosity parameter (K). In Fig. 7, it's evident that increasing K values result in a decline in the velocity profile, reflecting the heightened resistance of the porous medium attributed to its decreased permeability. This decrease in permeability leads to a reduction in fluid velocity. Additionally, Fig. 8 showcases the rise in fluid temperature as K increases, while Fig. 9 illustrates the accompanying decrease in the concentration profile. Figs. 10-12 exhibit how the unsteadiness parameter (A) influences $f'(\eta)$, $\theta(\eta)$ and $\phi(\eta)$ profiles. In Fig. 10, a decrease in fluid velocity is observed with increasing A, attributed to the reduction in heat transported to the sheet as A increases.

Moreover, Fig. 11 illustrates that fluid temperature decreases as A accelerates. Conversely, Fig. 12 demonstrates an increase in the concentration profile with rising A values. Figs. 13-14 represent the sway of Prandtl number on $\theta(\eta)$ and $\phi(\eta)$ profiles respectively. The values of Prandtl number $Pr = 0.71, 1.38, 4, 7.56$ stand for air, gaseous ammonia, R-12 refrigerant and water at 18° respectively. Kinematic viscosity to thermal diffusivity is the ratio that determines the Prandtl number. Fluid temperature (Fig. 13) is found to decrease as Pr attains higher values. Fig. 14 makes it clear that an increase in radiation parameter (R) causes the fluid temperature to accelerate. Fig. 15 depicts the effect of Eckert number(Ec) on temperature profile. Higher values of Ec elevate fluid temperature. The association between the specific enthalpy difference between a sheet and a fluid and its kinetic energy is known as the Eckert number. This temperature elevation occurs due to the escalation of Eckert number, primarily attributed to the augmentation of frictional heating in the fluid. The influence of joule heating parameter (H) on temperature is illustrated in Fig. 16. An upturn in H enhances fluid temperature profile. The energy that is mechanically converted into thermal energy by the internal friction of molecules is what raises the temperature. Figs. 17 and 18 indicate the influence of Brownian motion parameter(Nb) on temperature and nano particle concentration profiles. It is evident from Fig. 21 that an increase in Nb values results in an upswing in the temperature profile. It is observed from Fig. 22 that rising Nb entails a decrease in the nano particle boundary layer thickness and as a results nano particle concentration profile reduces. The effect of Nton $\theta(\eta)$ and $\phi(\eta)$ profiles are discussed in Figs. 19 and 20. It is seen that both fluid temperature and nano particle concentration profile enhance with rising values of Nt. Increases in Nt cause the thermophoresis force, which is responsible for transporting nanoparticles from hot to cold regions, to rise. This raises both fluid temperature and concentration profile of nanoparticles. The consequence of A_1on $\theta(\eta)$ profileis exposed in Fig. 21. Increasing the values of $A_1 > 0$ elevates the fluid temperature whereas an opposite trend is observed for space dependent heat sink parameter $(A_1 < 0)$. Fig. 22 depicts how changes in the time-dependent heat source or sink parameter (B_1) affect the $\theta(\eta)$ profile. Specifically, augmenting $B_1 > 0$ values result in higher fluid temperatures whereas a reverse trend is observed for the space-dependent heat sink parameter $(B_1 < 0)$. Figs. 23-25 are sketched to scrutinize the effect of Lewis number (Le), chemical reaction parameter (γ) and Soret number (S_r)on nano particle concentration profile respectively. Similar effect is seen for Le and γ that is, nano particle concentration profile decreases for improvement in values of them. Fig. 25 shows the escalation of $\phi(\eta)$ for improvement in values of S_r. The Soret effect's role in the temperature gradient-induced species migration from lower to higher solute concentrations that is why $\phi(\eta)$ enhances. The influence of suction or blowing parameter on $f'(\eta)$, $\theta(\eta)$ and $\phi(\eta)$ profiles are plotted in Figs. 26-28, respectively. The blowing parameter $(S < 0)$ exhibits a trend of boosting fluid velocity and temperature while concurrently diminishing the nano particle concentration profile. An opposite trend is observed for suction parameter $(S > 0)$.

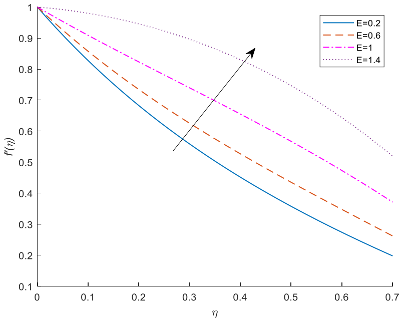

Fig. 1. Velocity profile $(f'(\eta))$ for E.

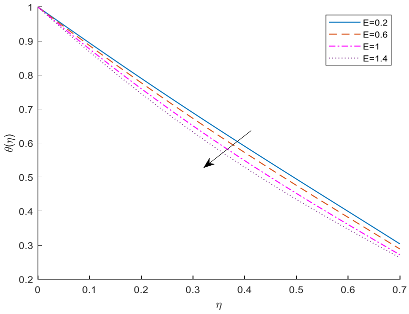

Fig. 2. Temperature profile $\left(\theta(\eta)\right)$ for E.

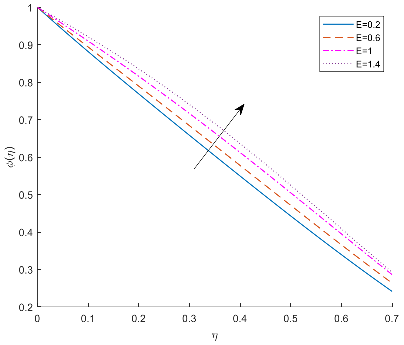

Fig. 3. Concentration profile$\left(\phi(\eta)\right)$ for E.

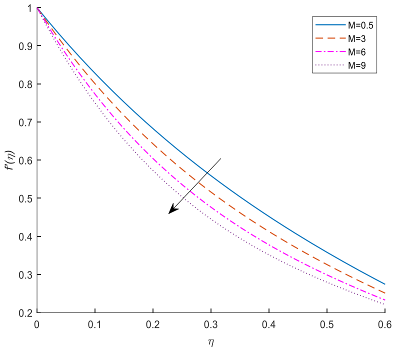

Fig. 4. $f'(\eta)$ for M.

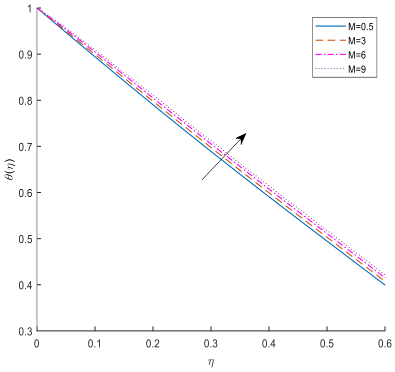

Fig. 5. $\theta(\eta)$ for M.

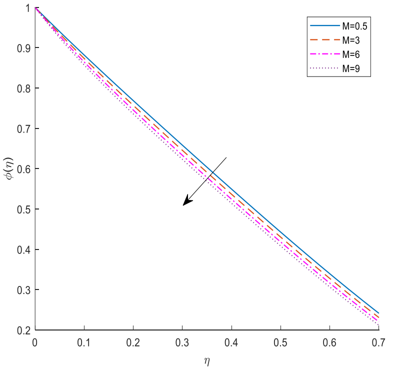

Fig. 6. $\phi(\eta)$ for M.

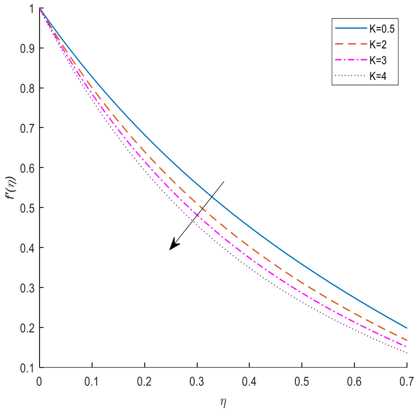

Fig. 7. $f'(\eta)$for K.

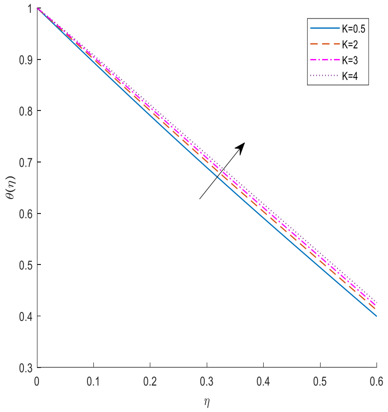

Fig. 8. $\theta(\eta)$ for K.

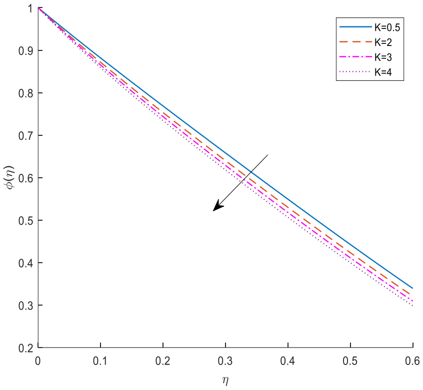

Fig. 9. $\phi(\eta)$ for K.

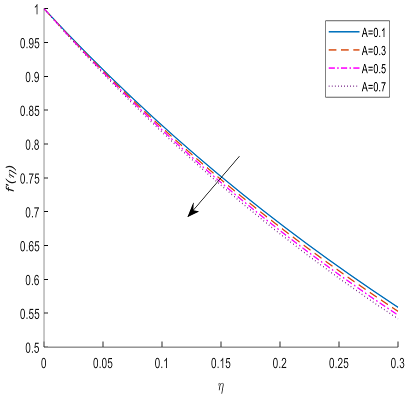

Fig. 10. $f'(\eta)$ for A.

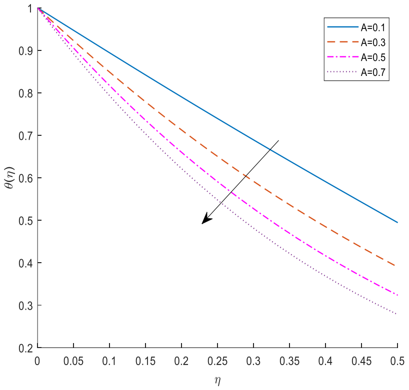

Fig. 11. $\theta(\eta)$ for A.

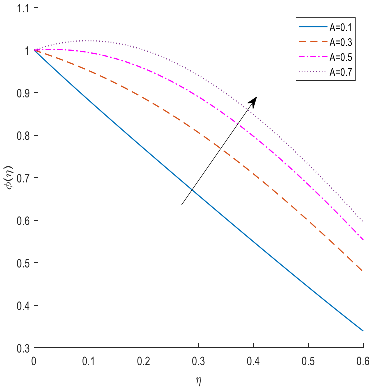

Fig. 12. $\phi(\eta)$ for A.

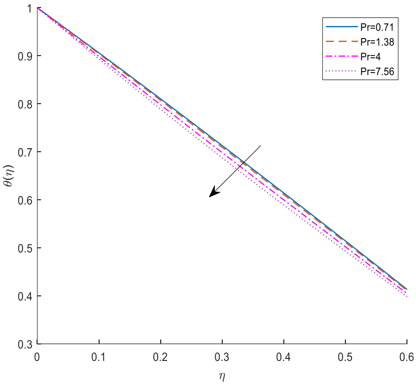

Fig. 13. $\theta(\eta)$ for Pr.

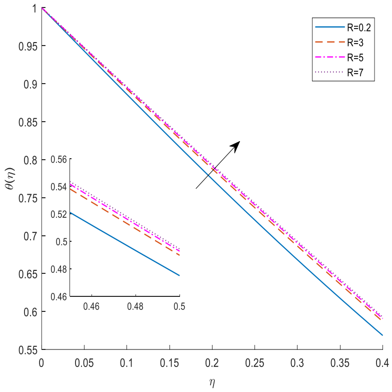

Fig. 14. $\theta(\eta)$ for R.

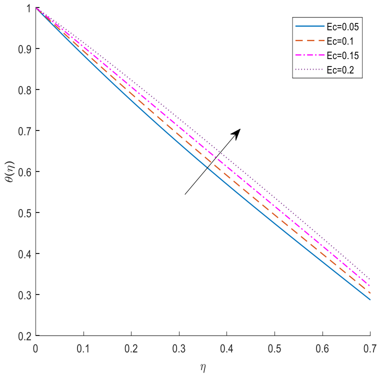

Fig. 15. $\theta(\eta)$ for Ec.

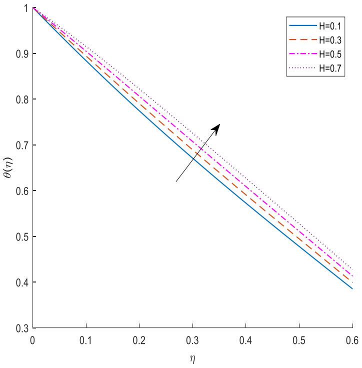

Fig. 16. $\theta(\eta)$ for H.

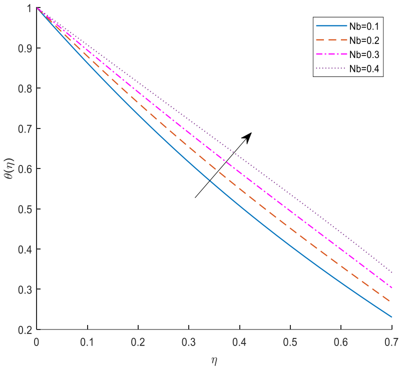

Fig. 17. $\theta(\eta)$ for Nb.

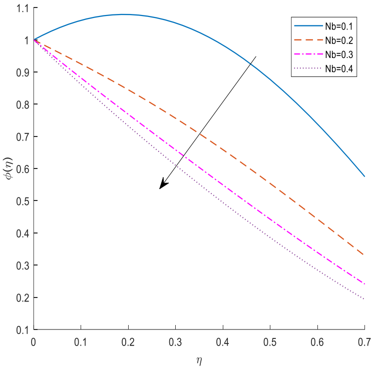

Fig. 18. $\phi(\eta)$ for Nb.

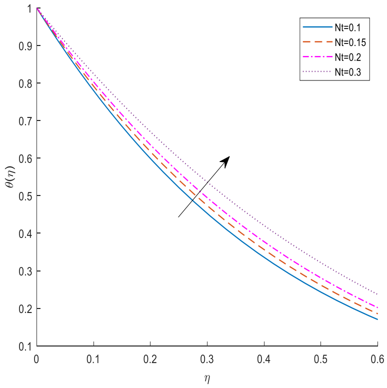

Fig. 19. $\theta(\eta)$ for Nt.

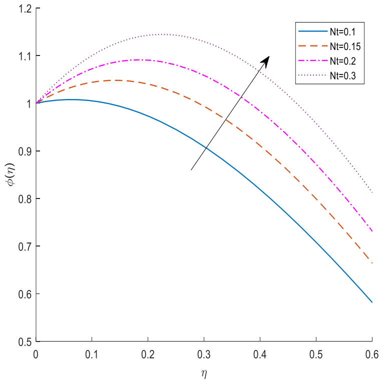

Fig. 20. $\phi(\eta)$ for Nt.

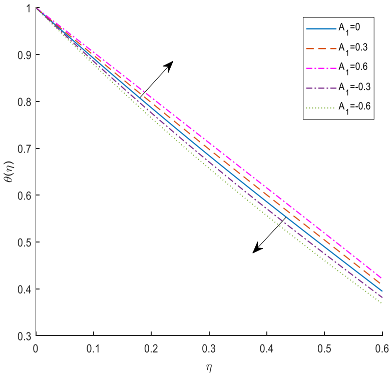

Fig. 21. $\theta(\eta)$ for A_1.

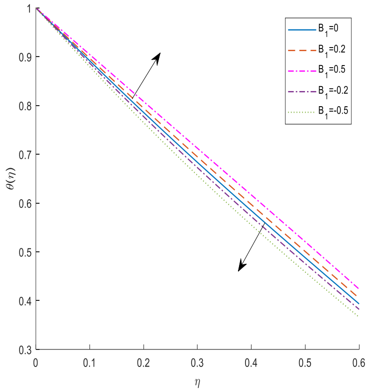

Fig. 22. $\theta(\eta)$ for B_1.

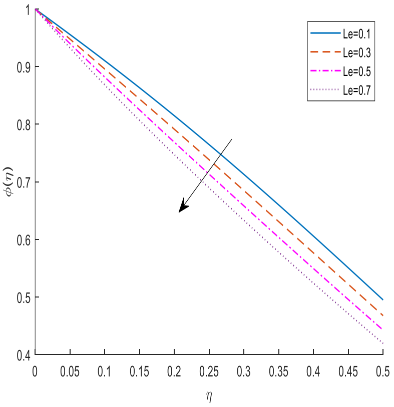

Fig. 23. $\phi(\eta)$ for Le.

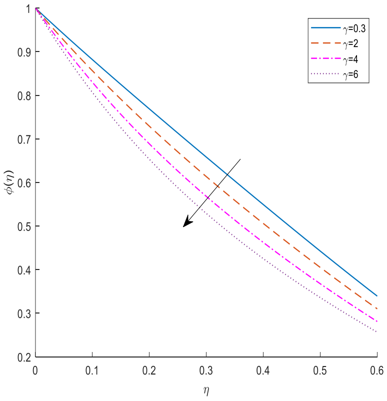

Fig. 24. $\phi(\eta)$ for γ.

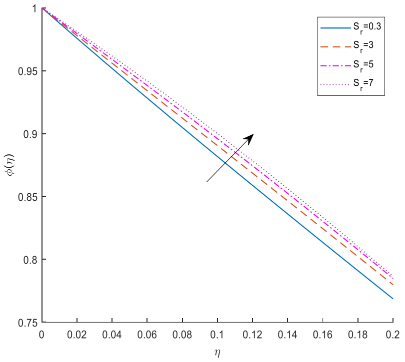

Fig. 25. $\phi(\eta)$ for S_r.

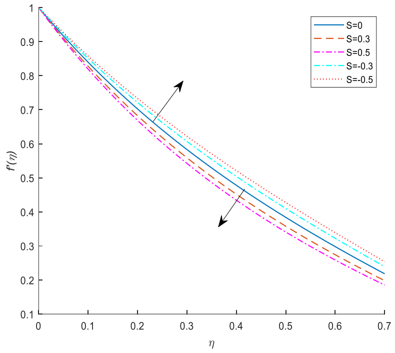

Fig. 26. $f'(\eta)$ for S.

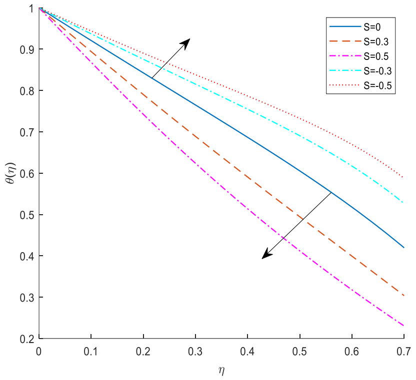

Fig. 27. $\theta(\eta)$ for S.

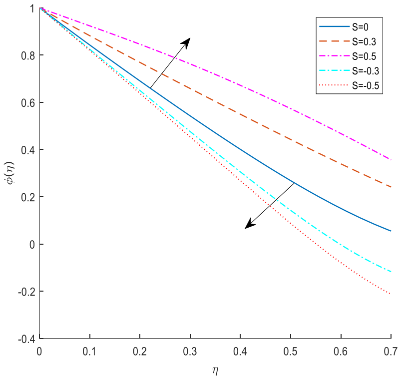

Fig. 28. $\phi(\eta)$ for S.

Tables 3-5 present a comprehensive breakdown of numerical values corresponding to the skin friction coefficient, Nusselt number, and Sherwood number across a range of modified parameters. Table 3 demonstrates a clear trend: as the E values escalate, the skin friction coefficient follows suit, whereas it diminishes as the A, M, K, and S values increase. It is also observed from Tables 3-4 that Nusselt number accelerates due to increase in $E, A, S(>0)$ and Pr and decelerates due to increase in $M, K, S(<0), R, Ec, H, A_1, B_1, Nb$ and Nt. Further, it is noticed from Tables 3-5 that Sherwood number diminishes for $E, A, S(>0), S_r$ and augments for $M, K, S(<0), Le$ and γ.

Table 3. Values of $f''(0), -\theta'(0)$ and $-\phi'(0)$ for different values of E, A, M, K, S.

Parameter	Values	$f''(0)$	$-\theta'(0)$	$-\phi'(0)$
E	0.6	-1.5425	1.1541	1.0731
	1	-0.9515	1.2729	0.8832
	1.4	-0.1298	1.3624	0.7550
A	0.3	-1.9297	1.5873	0.4155
	0.5	-1.9724	1.9654	-0.1044
	0.7	-2.0133	2.2568	-0.4590
	0.1	-1.8212	1.0756	1.2025

M	0.2	-1.8373	1.0724	1.2078
	0.3	-1.8533	1.0692	1.2132
K	0.1	-1.7875	1.0851	1.1866
	0.2	-1.8122	1.0796	1.1959
	0.3	-1.8367	1.0740	1.2052
S	−0.5	-1.5198	0.5688	1.8039
	−0.3	-1.6041	0.6374	1.7696
	0.3	-1.8851	1.0629	1.2238
	0.5	-1.9882	1.3362	0.7802

Table 4. Values of $-\theta'(0)$ for different values of governing parameters.

Parameter	Values	$-\theta'(0)$
Pr	0.71	1.4621
	1.38	1.4236
	4	1.3085
R	3	1.0803
	5	1.0594
	7	1.0470
Ec	0.05	1.1905
	0.1	1.0629
	0.15	0.9357
H	0.1	1.1960
	0.3	1.0629
	0.5	0.9302
A_1	−0.3	1.1632
	−0.6	1.2385
	0.3	1.0129
	0.6	0.9380
B_1	−0.2	1.1464
	−0.5	1.2279
	0.2	1.0346
	0.5	0.9481
Nb	0.1	1.4227
	0.2	1.2295
	0.3	1.0629
Nt	0.1	2.4093
	0.2	2.1148
	0.3	1.8530

Table 5. Values of $-\phi'(0)$for various controlling parameter values.

Parameter	Values	$-\phi'(0)$
Le	0.1	0.8769
	0.3	1.0873
	0.5	1.2238
γ	2	1.5455
	4	1.8820
	6	2.1826
S_r	3	1.1100
	5	1.0200
	7	0.9345

5. Conclusion

The current investigation addresses the computerized solution of the unsteady MHD stagnation boundary layer flow, heat, and mass transfer of an incompressible viscous micro fluid. A system of ODEs is created from the linked PDEs, and these ODEs are then numerically solved in MATLAB using bvp4c. The core consequences are the nano particle concentration profile reduces due to an improvement in the Lewis number and chemical reaction parameter, respectively and rises due to an improvement in the Soret number. Enhancing the unsteadiness parameter reduces the coefficient of skin friction and mass transfer rate and increase heat transfer rate. The acceleration in the values of velocity ratio parameter boots fluid velocity and concentration profile whereas reduces fluid temperature. Improving both the magnetic and porosity parameters leads to the temperature profile increasing, while simultaneously causing decreases in both the velocity and concentration profiles. Elevated thermophoresis, Eckert, joule heating, and radiation parameters lead to a rise in fluid temperature, whereas an increase in the Prandtl number causes it to decline. The concentration profile can be maximized by increasing thermophoresis parameter. This profile can also be minimized enhancing the Brownian motion parameter.

References

1. G. Vasumathi and J. A. Rao, J. Nanofluids **4**, 505 (2015). https://doi.org/10.1166/jon.2015.1180
2. S. U. Khan, S. A. Shehzad, A. Rauf, and N. Ali, Results Phys. **8**, 1223 (2018). https://doi.org/10.1016/j.rinp.2018.01.054
3. E. Haile and G. Awgichew, J. Nanofluids **8**, 1189 (2019). https://doi.org/10.1166/jon.2019.1678
4. S. U. Choi and J. A. Eastman, ASME **1995**, 231 (1995).
5. J. Cui, R. Razzaq, U. Farooq, W. A. Khan, F. B. Farooq, and T. Muhammad, Alexandria Eng. J. **61**, 4253 (2022). https://doi.org/10.1016/j.aej.2021.09.045
6. B. C. Prasannakumara, J. K. Madhukesh, and G. K. Ramesh, Propulsion Power Res. **12**, 284, (2023). https://doi.org/10.1016/j.jppr.2023.05.004
7. M. Amjad, M. N. Khan, K. Ahmed, I. Ahmed, T. Akbar, and S. M. Eldin, Case Studies in Thermal Eng. **45**, ID 102900 (2023). https://doi.org/10.1016/j.csite.2023.102900
8. M. D. Shamshuddin, S. O. Salawu, K. Ramesh, V. S. Patil and P. Humane, J. Thermal Anal. Calormetry **148**, 12083 (2023). https://doi.org/10.1007/s10973-023-12465-x
9. K. Ramesh, K. K. Asogwa, T. Oreyeni, M. G. Reddy, and A. Verma, Biomass Conv. Biorefin. **14**, 18887 (2024). https://doi.org/10.1007/s13399-023-04033-y
10. N. F. Dzulkifli, N. Bachok, N. A. Yacob, N. M. Arifin, and H. Rosali, Appl. Sci. **8**, 2172 (2018). https://doi.org/10.3390/app8112172
11. I. Rashid, M. Sagheer, and S. Hussain, Phys. Scripta **95**, ID 025027 (2020). https://doi.org/10.1088/1402-4896/ab444d
12. I. Waini, S. Pop, A. Bakar, and A. Ishak, Int. J. Numer. Meth. Heat Fluid Flow **32**, 1012 (2022). https://doi.org/10.1108/HFF-01-2021-0039
13. Z. Mahmood, S. E. Alhazmi, A. Alhowaity, R. Marzouki, N. Al-Ansari, and U. Khan, Sci. Report **12**, ID 16020 (2022). https://doi.org/10.1038/s41598-022-20074-1
14. M. S. Khan, I. Karim, L. E. Ali, and A.I slam, Int. Nano Lett. **2**, ID 24 (2012). https://doi.org/10.1186/2228-5326-2-24
15. Y. S. Daniel, Z. A. Aziz, Z. Ismail, and F. Salah, Alexandria Eng. J. **57**, 2187 (2018). http://dx.doi.org/10.1016/j.aej.2017.07.007
16. J. K. Zhang, B. W. Li, and Y. Y. Chen, J. Heat Transfer **137**, ID 052502 (2015). https://doi.org/10.1115/1.4029681
17. J. K. Madhukesh, G. K.Ramesh, E. H. Aly, and A. J. Chamkha, Alexandria Eng. J. **61**, 2418 (2022). https://doi.org/10.1016/j.aej.2021.06.104
18. A. Sinha, J. C. Misra, and G. C. Shit, Alexandria Eng. J. **55**, 2023 (2016). http://dx.doi.org/10.1016/j.aej.2016.07.010
19. M. M. Nandeppanavar, K. Vajravelu, and M. S. Abel, Commun. Nonlinear Sci. Numer. Simulat. **16**, 3578 (2011). https://doi.org/10.1016/j.cnsns.2010.12.033
20. B. Ramandevi, J. R. Reddy, V. Sugunamma, and N. Sandeep, Alexandria Eng. J. **57**, 1009 (2018). https://doi.org/10.1016/j.aej.2017.01.026

21. F. M. Hady, F. S. Ibrahim, S. M. Abdel-Gaied, and M. R. Eid, Nanoscale Res. Lett. **7**, ID 229 (2012). https://doi.org/10.1186/1556-276X-7-229
22. R. Akter and M. A. Islam, J. Sci. Res. **15**, 621 (2023). http://doi.org/10.3329/jsr.v15i3.63523
23. M. Sheikh and Z. Abbas, J. Magnet. Magnet. Mater. **396**, 204 (2015). https://doi.org/10.1016/j.jmmm.2015.08.011
24. M. Irfan and M.A. Farooq, J. Mater. Res. Technol. **9**, 4855 (2020). https://doi.org/10.1016/j.jmrt.2020.03.005
25. M. B. K. Moorthy and K. Senthilvadivu, J. Appl. Math. **2012** (2012). https://doi.org/10.1155/2012/634806
26. Y. S. Daniel, Z. A. Aziz, Z. Ismail, and F. Salah, J. King Saud Univ.-Sci. **31**, 804 (2019). https://doi.org/10.1016/j.jksus.2017.10.002
27. K. Raghunath, J. Nanofluids **12**, 767 (2023). https://doi.org/10.1166/jon.2023.1965
28. D. Gohain, R. Bordoloi, and N. Ahmed, J. Nanofluids **12**, 1804 (2023). https://doi.org/10.1166/jon.2023.2058
29. G. V. Kumar, K. U. Rehman, R. V. M. S. S. K. Kumar, and W. Shatanawi, Waves in Random and Complex Media 1 (2022). https://doi.org/10.1080/17455030.2022.2072531
30. M. A. Islam, M. Y. Ali, and S. M. O Gani, J. Sci. Res. **14**, 443 (2022). http://dx.doi.org/10.3329/jsr.v14i2.55577
31. M. A. Islam, M. Y. Ali, R. Akter, and S. M. O Gani, J. Appl. Math. Phys. **10**, 3016 (2022). https://doi.org/10.4236/jamp.2022.1010202
32. M. Q. Brewster, Thermal Radiative Transfer and Properties (John Wiley & Sons, 1992).